Structural maturation of cortical perineuronal nets and their perforating synapses revealed by superresolution imaging

Yaron M. Sigal[a,b,c], Haneui Bae[d,e], Luke J. Bogart[d,e], Takao K. Hensch[d,e,f,g,1], and Xiaowei Zhuang[a,b,c,d,g,1]

[a]Howard Hughes Medical Institute, Harvard University, Cambridge, MA 02138; [b]Department of Chemistry and Chemical Biology, Harvard University, Cambridge, MA 02138; [c]Department of Physics, Harvard University, Cambridge, MA 02138; [d]Center for Brain Science, Harvard University, Cambridge, MA 02138; [e]Department of Molecular and Cellular Biology, Harvard University, Cambridge, MA 02138; [f]F. M. Kirby Neurobiology Center, Department of Neurology, Boston Children's Hospital, Harvard Medical School, Boston, MA 02115; and [g]National Institute of Mental Health (NIMH) Silvio O. Conte Center, Harvard University, Cambridge, MA 02138

Contributed by Xiaowei Zhuang, February 14, 2019 (sent for review October 8, 2018; reviewed by Joerg Bewersdorf and Tommaso Pizzorusso)

Parvalbumin-positive (PV+) interneurons play a pivotal role in orchestrating windows of experience-dependent brain plasticity during development. Critical period closure is marked by the condensation of a perineuronal net (PNN) tightly enwrapping subsets of PV+ neurons, both acting as a molecular brake on plasticity and maintaining mature PV+ cell signaling. As much of the molecular organization of PNNs exists at length scales near or below the diffraction limit of light microscopy, we developed a superresolution imaging and analysis platform to visualize the structural organization of PNNs and the synaptic inputs perforating them in primary visual cortex. We identified a structural trajectory of PNN maturation featuring a range of net structures, which was accompanied by an increase in Synaptotagmin-2 (Syt2) signals on PV+ cells suggestive of increased inhibitory input between PV+ neurons. The same structural trajectory was followed by PNNs both during normal development and under conditions of critical period delay by total sensory deprivation or critical period acceleration by deletion of *MeCP2*, the causative gene for Rett syndrome, despite shifted maturation levels under these perturbations. Notably, superresolution imaging further revealed a decrease in Syt2 signals alongside an increase in vesicular glutamate transporter-2 signals on PV+ cells in *MeCP2*-deficient animals, suggesting weaker recurrent inhibitory input between PV+ neurons and stronger thalamocortical excitatory inputs onto PV+ cells. These results imply a latent imbalanced circuit signature that might promote cortical silencing in Rett syndrome before the functional regression of vision.

parvalbumin interneuron | critical period | visual cortex | dark rearing | MeCP2

Individual brain regions are highly malleable in response to environmental stimuli during early windows of development, termed critical periods. These critical periods are staggered in time across the brain, with primary sensory areas of the neocortex maturing earlier than those performing higher-order integration such as language (1). At a cellular level, subsets of interneurons expressing the calcium-binding protein parvalbumin (PV) play an essential role in timing critical period plasticity (2, 3). These PV-positive (PV+) cells are themselves first to respond to sensory deprivation (2), and their highly interconnected networks further synchronize high-frequency gamma oscillations that are correlated with active cognition, learning, and memory (4). Defects in PV+ circuits, gamma oscillations, and critical period timing have been implicated in numerous mental disorders (5, 6).

Maturation of these PV+ cells is accompanied by the condensation of an extracellular matrix—the perineuronal net (PNN), which forms a mesh-like structure perforated by synapses, surrounding the somata and proximal neurites of these cells (7–9). The condensed PNN is thought to act as a molecular brake on synaptic plasticity as critical periods close (10, 11), and cleavage of PNN components can partially reopen plasticity in adulthood (12, 13). Abnormal PNNs are a hallmark of cognitive disability, ranging from accelerated accumulation in certain neurodevelopmental disorders (14, 15) to their dissolution in schizophrenia (16). Various physiological roles have been suggested for PNNs including receptor stabilization (17), molecular signaling (18, 19), and protection against oxidative stress (20, 21). Recently, it has been proposed that PNNs might act as a synaptic "punch card" for long-term memory (22), a hypothesis that remains to be experimentally tested. Despite the physiological importance of the PNNs, our understanding of their structural development and function remains limited, due in part to the challenges associated with imaging the nanoscale organization of the brain extracellular matrices and their relation to synapses.

Here, we combined stochastic optical reconstruction microscopy (STORM) (23) with serial-section reconstruction (24, 25) to facilitate large-volume, 3D superresolution fluorescence imaging. We applied this approach to examine both the structural organization of PNNs and their penetrating synaptic inputs onto PV+ cells in mouse primary visual cortex with nanometer-scale resolution. Our superresolution data revealed a structural trajectory of PNN maturation that is followed both during normal development and under physiologically and medically relevant perturbations, despite the associated shifts in critical period timing by these perturbations. Furthermore, our superresolution images also uncovered a defect in inhibitory synaptic connectivity between PV+

Significance

Particular inhibitory neurons containing parvalbumin (PV) play a critical role in determining the time course by which experience shapes developing brain circuits. Embedded deep within cortical gray matter, extracellular matrices enwrapping PV-positive (PV+) cells have remained difficult to study partly due to the small length scale on which they are organized. To overcome such challenges, we used a superresolution fluorescence imaging approach to visualize these perineuronal nets (PNNs), a specialized form of the extracellular matrix critical for maintaining mature PV+ neuron function and their synaptic inputs. We quantified changes that define PNN structure and identified specific synaptic defects in a mouse model lacking *MeCP2*, the causative gene for Rett syndrome, a regressive neurodevelopmental disorder.

Author contributions: Y.M.S., T.K.H., and X.Z. designed research; Y.M.S., H.B., L.J.B., T.K.H., and X.Z. performed research; Y.M.S. contributed new reagents/analytic tools; Y.M.S. analyzed data; and Y.M.S., T.K.H., and X.Z. wrote the paper.

Reviewers: J.B., Yale School of Medicine; and T.P., University of Florence.

The authors declare no conflict of interest.

[1]To whom correspondence may be addressed. Email: hensch@mcb.harvard.edu or zhuang@chemistry.harvard.edu.

This article contains supporting information online at www.pnas.org/lookup/suppl/doi:10.1073/pnas.1817222116/-/DCSupplemental.

Published online March 19, 2019.

neurons in mice lacking *MeCP2*, the causative gene for Rett syndrome, an autism-like neurodevelopmental disorder (26, 27).

Results

Structural Characterization of PNNs with Serial-Section STORM Imaging. To visualize PV+ interneurons and their surrounding PNNs in mouse primary visual cortex (V1), we imaged four molecular markers in each sample simultaneously: (*i*) an antibody against PV to recognize PV+ cells; (*ii*) *Wisteria floribunda* agglutinin (WFA), a plant lectin which specifically binds to chondroitin sulfate proteoglycans, major components of the PNN (28); (*iii*) wheat germ agglutinin (WGA), a lectin marker used for serial-section alignment (25); and (*iv*) antibodies against synaptic markers, including an excitatory synapse marker—vesicular glutamate transporter-2 (VGLUT2)—a transmembrane protein which loads glutamate into excitatory synaptic vesicles and primarily localizes to thalamic inputs to the cortex in adult mice (29), or an inhibitory synapse marker—Synaptotagmin-2 (Syt2)—a calcium sensor that is involved in synaptic vesicle release and localizes to presynaptic inhibitory terminals of cortical PV+ cells (30, 31).

After labeling each tissue sample and embedding it in epoxy-based resin, we collected ∼300 serial sections (each 70 nm in thickness) through thalamorecipient layer 4 of V1 and imaged them on a serial-section STORM platform that we developed previously (25) but substantially improved here (*SI Appendix, Materials and Methods*). STORM is a single-molecule-based superresolution imaging method, which achieves subdiffraction-limit image resolution by stochastic activation and precise localization of individual photoswitchable fluorescent molecules (23). The combination of serial ultrathin sectioning with STORM allows large-volume superresolution reconstruction of tissue samples without resolution deterioration due to tissue-induced aberration (25). Here, by using stronger lasers, a faster camera, and improved automation in image acquisition, we increased the imaging speed of the serial-section STORM platform by 10-fold, allowing regions spanning ∼100 × 100 × 20 μm in volume (∼300 serial sections) and containing multiple PV+ cells to be routinely imaged and reconstructed within a day (Fig. 1*A* and *SI Appendix, Materials and Methods* and Fig. S1 *A* and *B*). This improvement made it feasible to image many neurons across multiple developmental time points and distinct perturbation conditions.

Our superresolution reconstructions resolved structural features of WFA-labeled PNNs substantially more clearly than diffraction-limited imaging (Fig. 1*A*). As PNNs are 3D, shell-like structures that wrap around the PV+ cell bodies and proximal neurites, we performed a Behrmann equal-area cylindrical surface projection (similar to a world-map projection) for each WFA+ PV+ soma (Fig. 1*B* and *SI Appendix, Materials and Methods* and Figs. S1 *C–E* and S2). In this transformation, the WFA signal was first fit to a sphere and transformed into spherical coordinates (θ, φ, *r*). Next, the angular coordinates (θ, φ) were projected onto a cylindrical coordinate system (θ′, *z*′) using a Behrmann equal-areal projection, while the radial coordinate value (*r*) was maintained as a third orthogonal dimension (*Z*′) of the Behrmann projection (*SI Appendix, Materials and Methods*). To more accurately represent the nonspherical surface of the cell, a 2D spline of the WFA surface signal was then fit to the WFA signal in the initial Behrmann projection and subtracted from the WFA signal in the *Z*′ dimension to give the local height above or below the surface (*SI Appendix, Materials and Methods*). This modified Behrmann projection thus created a flattened surface which allowed us to present the observed PNN and synaptic signals in two dimensions with better clarity than in 3D Cartesian coordinates.

Structural Organization of PNNs at Different Developmental Stages. First, we imaged PV+ cells in layer 4 of adult mouse V1 at postnatal day 90 (P90) (Fig. 1*C*; $n = 44$ cells). As most of the PV+ cells were observed to be WFA+ and most of the WFA+ cells were also observed to be PV+ (*SI Appendix, Materials and Methods*), we focused our analysis on WFA+ PV+ cells. We observed a wide range of WFA signal strengths across different cells, spanning more than one order of magnitude in intensity. The morphology of PNNs varied widely, from a sparse, disconnected pattern to an entirely contiguous net structure. Increases in the average WFA signal intensity across the entire cell surface (including both WFA-positive and WFA-negative regions on the cell surface), hereafter termed the WFA surface intensity, resulted from both a higher mean intensity within WFA+ regions as well as an increased fraction of surface area that was WFA+ (*SI Appendix,*

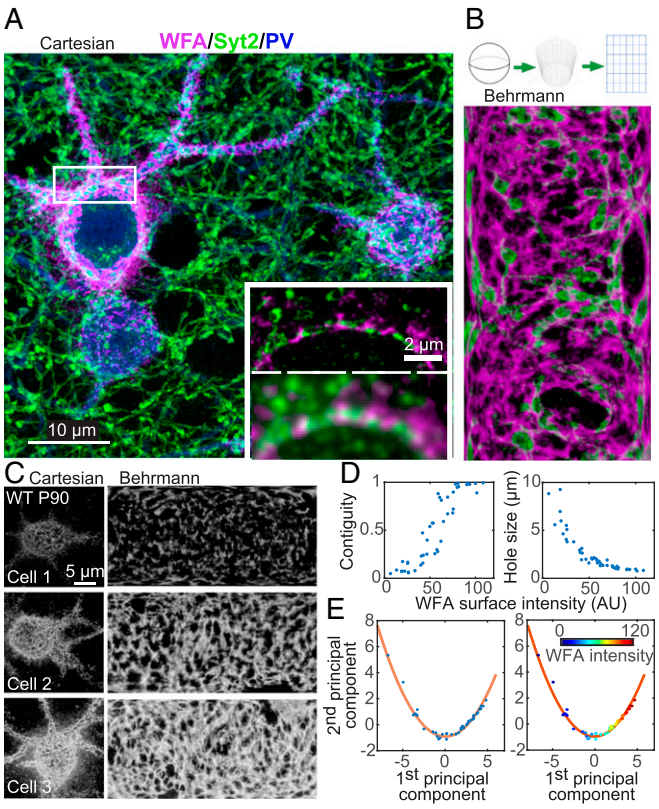

Fig. 1. Structural characterization of the PNN with serial-section superresolution STORM imaging. (*A*) Representative maximum-intensity projection STORM image through 6 μm of tissue centered around layer 4 of the mouse primary visual cortex, V1 (magenta, WFA; green, Syt2; blue, PV). (Scale bar, 10 μm.) (*A*, *Inset*) Comparison of conventional (*Bottom*) and STORM (*Top*) images of a single 70-nm section in the boxed region. (Scale bar, 2 μm.) (*B*) Behrmann equal-area cylindrical surface projection of the PNN ensheathing a PV+ cell and inhibitory synapses perforating the PNN. (*B*, *Top*) Schematic of the projection method (*SI Appendix, Materials and Methods*). (*B*, *Bottom*) Behrmann equal-area cylindrical surface projection of WFA (magenta) and Syt2 (green) signals of a 500-nm-thick region centered around the radial peak of the WFA signal surrounding a PV+ cell. (*C*) Three representative examples of WFA+ PV+ cells with increasing WFA intensities from wild-type P90 mice. (*C*, *Left*) Maximum-intensity projection STORM images of WFA in Cartesian coordinates. (*C*, *Right*) Behrmann equal-area cylindrical surface projections through a 500-nm-thick region centered around the radial peak of the WFA signal. (*D*) Bivariate plots of the contiguity of the WFA signal (*Left*) and the hole size in the PNN (*Right*) versus WFA surface intensity. Each dot represents a single imaged cell. WFA surface intensity is defined as the mean intensity of the WFA signal across the entire cell surface for each cell. Contiguity is defined as the fraction of the WFA signal in the largest connected component for each cell. Hole size is defined as the mean effective radius of the holes in the PNN for each cell. (*E*) Principal component analysis for structural metrics of PNNs around WFA+ PV+ cells in P90 animals. Metrics of the PNN structure, including WFA surface intensity, contiguity, and hole size, as defined here, as well as five other metrics as defined in *SI Appendix*, Fig. S3, are used in the principal component analysis. (*E*, *Left*) The first two components of the principal component analysis are plotted for individual P90 cells (blue dots) and fit to a quadratic function (red line). (*E*, *Right*) Same as *Left*, but with dots color-coded according to the WFA surface intensity for each cell.

Fig. S3*A*). We found the contiguity of the PNN structure correlated strongly with the WFA surface intensity (Spearman correlation coefficient, $\rho = 0.94$; Fig. 1*D*) and, consequently, cells with stronger WFA surface intensity also had smaller, more uniform "holes" within the PNN, with a mean hole size that was inversely correlated with the WFA surface intensity (Spearman correlation coefficient, $\rho = -0.97$; Fig. 1*D*). The cell body shape, on the other hand, was not correlated with the WFA surface intensity (*SI Appendix*, Fig. S2).

To collectively consider the PNN continuity and hole size, as well as several other structural aspects of PNNs (*SI Appendix*, Fig. S3*A*), we performed a principal component analysis of all these metrics for individual WFA+ PV+ cells (Fig. 1*E*). The first principal component showed positive correlation with WFA surface intensity, contiguity, and inverse hole size (*SI Appendix*, Fig. S3*B*), reflecting the maturation level of the PNNs. Thus, this first principal component could be considered a "pseudotime" axis, and the relation between the first and second principal components represented a structural trajectory of PNN maturation (Fig. 1*E*). This description of PNN structural variation in adult wild-type animals set a baseline for comparison across different developmental stages and different sensory or genetic perturbations.

We next examined layer 4 of V1 in younger wild-type animals at P30, which is the height of the critical period for plasticity of visual acuity (2, 3) (Fig. 2*A*; $n = 33$ cells). As expected for less mature PNNs, overall WFA signals surrounding PV+ cells were weaker than in adult P90 animals (Fig. 2*B*). The younger PNNs still displayed a wide range of surface intensities, contiguity, and hole sizes, partially overlapping those observed at P90 (Fig. 2*B* and *SI Appendix*, Fig. S4*A*). Notably, principal component analysis of the P30 cells fell along the same trajectory as those at P90, but with lower values overall along the first principal component (Fig. 2*C*), consistent with the notion that this structural trajectory identifies a pseudotime representation of PNN maturation.

Structural Organization of PNNs Under Perturbations That Shift Critical Period Timing. We then considered two different conditions known to shift onset timing of the critical period. The first was full sensory deprivation: Mice raised in total darkness from birth delay the onset of visual plasticity until introduced into a standard light/dark cycle regardless of age (2, 32, 33). We imaged layer 4 in V1 tissues collected from dark-reared (DR) mice at P90 compared with the age-matched, normally raised adults described above (Fig. 3*A*; $n = 50$ cells). The density of PNN-enwrapped PV+ cells (WFA+ PV+ cells) was slightly decreased compared with age-matched controls, consistent with previous findings that PNNs are slightly less abundant in layer 4 of DR animals (13).

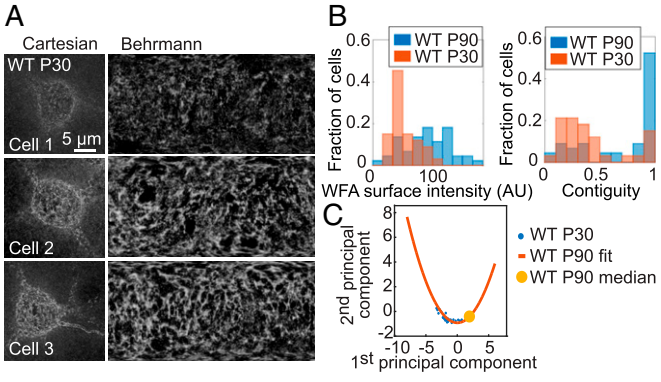

Fig. 2. Structural trajectory of PNN maturation. (*A*) PNN images of three representative examples of WFA+ PV+ cells in wild-type mice at P30. (*A*, *Left*) Maximum-intensity projection STORM images of WFA in Cartesian coordinates. (*A*, *Right*) Behrmann equal-area cylindrical surface projections. (*B*) Probability distributions of WFA surface intensity (*Left*) and PNN contiguity (*Right*) at P90 (blue) and P30 (red). (*C*) Principal component analysis for structural metrics of PNNs around WFA+ PV+ cells in P30 animals. The first two principal components are plotted (blue dots) for individual P30 cells together with the quadratic fit function obtained for P90 cells (red line; reproduced from Fig. 1*E*). The median value of the P90 data is also shown for reference (yellow circle).

Of these cells, DR samples showed on average moderately less developed PNNs as measured by WFA surface intensity, contiguity, and mean hole size (Fig. 3*B* and *SI Appendix*, Fig. S4*B*). Notably, principal component analysis of the data from DR animals once again fell along the same trajectory as that derived from normally raised animals, with only a moderately lower degree of maturation on average (Fig. 3*C*). This suggests that the morphology of those PNNs that do form in the dark did not deviate substantially from that of normally raised animals, except for the moderately lower PNN intensity. Consistent with this, the WFA signal of DR samples further displayed a nearly identical radial profile to that of normally raised animals (*SI Appendix*, Fig. S4*D*).

The second perturbation that we examined was deletion of the *MeCP2* gene. In contrast to dark rearing, the absence of the *MeCP2* gene in male mice accelerates PV+ neuron development (34), leading to a precocious critical period entry accompanied by earlier appearance of PNNs (15). Heterozygous female patients carrying a mosaic loss-of-*MeCP2* function are diagnosed with Rett syndrome (26) and display alterations in visually evoked potentials and acuity in parallel with other regressive symptoms (27, 35). Here, we examined the more rapidly regressing homozygous *MeCP2* knockout males ($MeCP2^{-/y}$) at P30 before the onset of cortical symptoms (34). PNNs enwrapping PV+ cells appeared substantially more mature in V1 of these *MeCP2*-deficient animals, exhibiting a higher average WFA intensity, greater contiguity, and smaller hole sizes compared with age-matched wild-type controls (Fig. 3 *D* and *E* and *SI Appendix*, Fig. S4*C*; $n = 34$ cells). Once again, principal component analysis of the data from *MeCP2* mutants fell along the same trajectory as wild-type animals but exhibited an overall shift toward a more mature distribution at P30 as compared to age-matched wild-type animals (Fig. 3*F*). The radial profile of the WFA signal in $MeCP2^{-/y}$ cells was also identical to that of age-matched wild-type mice (*SI Appendix*, Fig. S4*D*).

Synaptic Contacts Perforating the PNN: Normal Development and Critical Period Perturbation. First, we examined inhibitory synaptic connections onto PNN-enwrapped PV+ cells using Syt2, an established marker specific to PV+ inhibitory axon terminals in the multiple regions of the cortex including V1 (30, 31). Syt2+ boutons were observed to contact the surface of PV+ cells, marking the reciprocal inhibitory contacts between PV+ cells (Fig. 4*A* and *SI Appendix*, Fig. S5*A*). These Syt2+ puncta resided primarily within the holes of the PNN and partially overlapped, at the edges, with WFA signals (Fig. 4*A*, *Top* and *SI Appendix*, Fig. S5 *A* and *B*). The mean surface intensity of Syt2 across the surface of PV+ cells increased with age (Fig. 4*B*), and was positively correlated with WFA surface intensity across development with a nonlinear scaling power of $\alpha = 0.65$, namely $I_{Syt2} \propto I_{WFA}^{0.65}$ (*SI Appendix*, Fig. S5*C*). Using this scaling relationship, we normalized Syt2 signals to the degree of PNN maturation for each individual cell, facilitating comparison across conditions (Fig. 4*B*). Examining across development, the WFA-normalized Syt2 surface intensity ($I_{Syt2}/I_{WFA}^{0.65}$) did not differ significantly between P30 and P90 mice (Fig. 4*B*). Interestingly, as WFA surface intensity increased, the fraction of Syt2 signals overlapping with the WFA signal at the bouton edge also increased (*SI Appendix*, Fig. S5*D*), suggesting that a larger portion of the inhibitory boutons may be physically pinned by the PNNs as the animal aged.

In DR animals, a similar correlation between the Syt2 surface intensity and the WFA surface intensity was observed, and the WFA-normalized Syt2 surface intensity was statistically indistinguishable from that of age-matched, normally raised animals (Fig. 4*B* and *SI Appendix*, Fig. S5 *A* and *C*). However, this trend was violated in the $MeCP2^{-/y}$ mice compared with age-matched controls. As the $MeCP2^{-/y}$ mice exhibited more mature PNNs bearing stronger WFA surface intensity (Fig. 3 *E* and *F*) and the Syt2 surface intensity was positively correlated with the WFA surface intensity (*SI Appendix*, Fig. S5*C*), one may predict a stronger Syt2

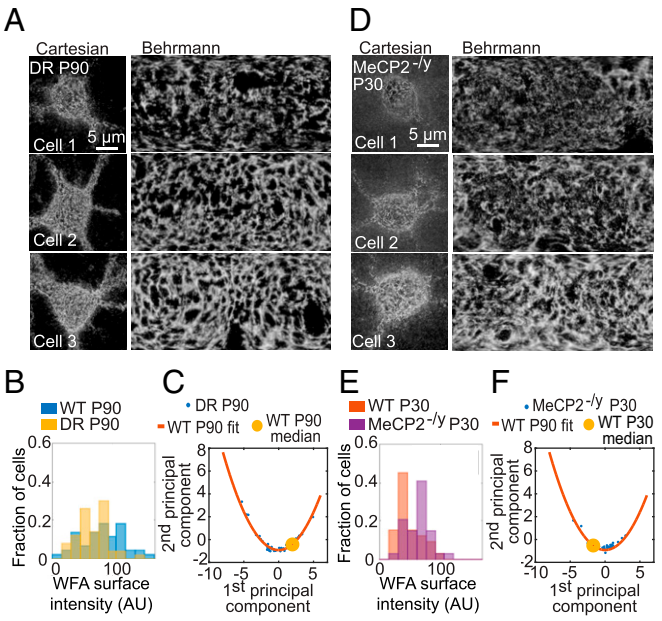

Fig. 3. Maturation of PNNs is shifted along a stereotypic trajectory in dark-reared or *MeCP2*-deficient mice. (*A*) PNN images of three representative examples of WFA+ PV+ cells in DR animals at P90. (*A*, *Left*) Maximum-intensity projection STORM images of WFA in Cartesian coordinates. (*A*, *Right*) Behrmann equal-area cylindrical surface projections. (*B*) Probability distribution of WFA surface intensity for the DR samples at P90 (yellow) in comparison with the age-matched control samples (blue). (*C*) Principal component analysis for structural metrics of PNNs around WFA+ PV+ cells from DR animals at P90. Data are plotted for individual cells (blue dots) in DR animals together with the quadratic fit function obtained from normally raised control P90 animals (red line; reproduced from Fig. 1*E*). The median value of the control P90 data is also shown for reference (yellow circle). (*D*–*F*) Same as *A*–*C* but for the *MeCP2*-deficient mice at P30, instead of the DR mice at P90, in comparison with age-matched wild-type control. In *F*, the quadratic fit function obtained from wild-type P90 animals is shown (red line, reproduced from Fig. 1*E*) and the median value of the wild-type P30 data is shown for reference (yellow circle).

surface intensity for MeCP2$^{-/y}$ samples compared with wild-type age-matched samples. Instead, these mutant animals had weaker Syt2 surface intensity and smaller physical sizes of the Syt2 clusters on their PV+ cells (Fig. 4*B* and *SI Appendix*, Fig. S5 *A*, *C*, *E*, and *F*). Accordingly, WFA-normalized Syt2 surface intensity showed an even more pronounced decrease in MeCP2$^{-/y}$ mice (Fig. 4*B*). These findings thus revealed an unexpected defect in PV–PV synaptic contacts in this animal model of accelerated critical period timing (15).

For comparison, we also studied the relationship between PNNs and excitatory synaptic inputs onto the same PV+ cells by examining VGLUT2, a known marker of thalamic presynaptic afferent terminals. VGLUT2 staining is strongest in layer 4 of the cortex (29), and VGLUT2+ boutons have been shown to contact PV+ neurons there (36). Indeed, in our samples, VGLUT2+ boutons were observed at the surface of PNN-enwrapped PV+ cells, again with contacts found primarily in the holes of the net (Fig. 4*A*, *Bottom* and *SI Appendix*, Fig. S6 *A* and *B*). In line with previous observations of more abundant inhibitory inputs compared with VGLUT2+ inputs onto PV+ somata (36), we observed more Syt2+ puncta than VGLUT2+ puncta at the surface of PV+ cells (*SI Appendix*, Fig. S6*C*). In contrast to the Syt2 signal, the mean VGLUT2 surface intensity onto PV+ cells decreased with age and was not correlated with WFA surface intensity (Fig. 4*C* and *SI Appendix*, Fig. S6 *A* and *D*). At WFA+ PV+ cells examined from MeCP2$^{-/y}$ animals, VGLUT2 surface intensity was even higher than on age-matched wild-type cells, and again was not correlated with WFA intensity (Fig. 4*C* and *SI Appendix*, Fig. S6 *A* and *D*).

The opposite age dependence of VGLUT2 and Syt2 signals suggests that PNN+ PV+ cells potentially shift toward stronger inhibitory input onto their cell somata as they mature. On the other hand, despite precocious PNN maturation in the MeCP2$^{-/y}$ animals, their PNN+ PV+ neurons have weaker Syt2 and stronger VGLUT2 surface intensities on their somata, potentially suggesting weaker inhibitory inputs and stronger excitatory inputs than in age-matched wild-type animals.

Morphological Defects of Syt2 Distribution in *MeCP2*-Deficient Animals. Returning to 3D Cartesian coordinates, we further observed a defect in the morphology of the Syt2 signal in MeCP2$^{-/y}$ animals. Wild-type P90, P30, and DR P90 samples all exhibited large continuous Syt2+ fibers connecting many axonal boutons surrounding the PV+ cells (Fig. 5*A*), indicating that Syt2 is distributed both in synaptic boutons and in the interbouton axonal regions. In contrast, MeCP2$^{-/y}$ P30 samples displayed primarily isolated Syt2+ boutons with interbouton regions along axons devoid of Syt2 signal (Fig. 5*A*). As a result, analyses of the Syt2 clusters yielded substantially smaller cluster sizes (centered at 10^{-1} μm^3, the expected size for one or two axonal boutons) and a drastically reduced fraction of Syt2 signal in the largest connected

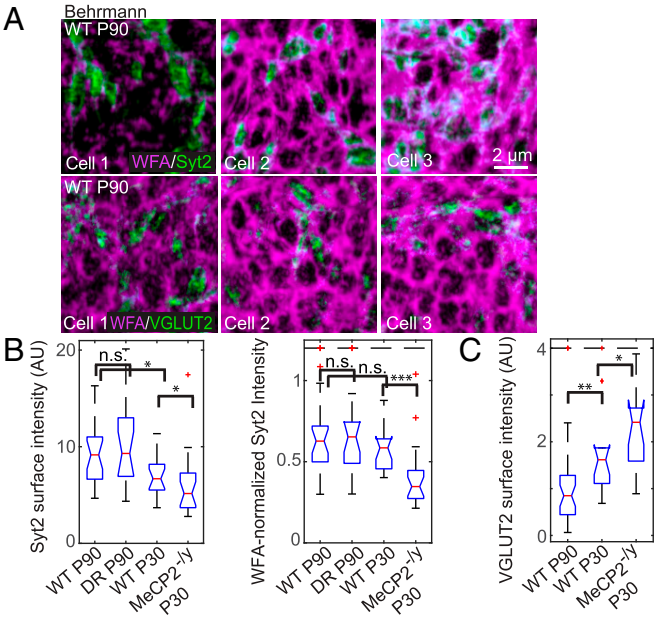

Fig. 4. Synaptic contacts perforating the PNN onto PV+ cells during normal development and in dark-reared or *MeCP2*-deficient mice. (*A*) Behrmann equal-area cylindrical surface projections of two-color STORM images of WFA (magenta) and synaptic proteins (green; Syt2 for *Top* and VGLUT2 for *Bottom*) in wild-type P90 animals. Only a representative portion of each cell is shown in each image. (Scale bar, 2 μm.) A scale bar is included for these small-area Behrmann projections, as the nonlinear distortion is relatively small over such a small area. (*B*) Box and whiskers plots for Syt2 surface intensity on individual WFA+ PV+ cells in animals across developmental and perturbation conditions: wild-type P90, WT P30, DR P90, and MeCP2$^{-/y}$ P30. Syt2 surface intensity is defined as the mean intensity of the Syt2 signal across the entire cell surface for each cell. (*B*, *Left*) Absolute Syt2 surface intensities. (*B*, *Right*) WFA-normalized Syt2 surface intensities ($I_{Syt2}/I_{WFA}^{0.65}$). Red lines denote median values; notches denote a 95% confidence interval around the median; boxes denote the first and third quartiles of the data; whiskers denote the expected 99% values assuming a normal distribution; outliers are shown as red crosses; and those above a cutoff threshold are shown as a dashed line. Statistical significance is determined by a two-sided Kolmogorov–Smirnov test. n.s., $P > 0.05$; *$P < 0.05$, **$P < 0.01$, ***$P < 0.001$. (*C*) Same as *B*, *Left* but for the VGLUT2 surface intensity instead of the Syt2 surface intensity. VGLUT2 surface intensity is defined as the mean intensity of the VGLUT2 signal across the entire cell surface for each cell.

component for the *MeCP2*-deficient animals compared with wild type (Fig. 5 *B* and *C*).

The above observations were not just limited to regions locally surrounding WFA+ PV+ cells. Across the entire imaged region of layer 4, we observed continuous distribution of Syt2 along the axonal shafts in wild-type P90, P30, and DR P90 samples (*SI Appendix*, Fig. S7). In MeCP2$^{-/y}$ P30 samples, such continuous distribution was disrupted in the entire imaged region of layer 4, which again exhibited largely isolated Syt2+ boutons (*SI Appendix*, Fig. S7).

In contrast to Syt2, VGLUT2 formed largely discrete boutons surrounding WFA+ PV+ cells across all imaged conditions (*SI Appendix*, Fig. S8*A*). While VGLUT2 clusters were less abundant at P90 than at P30 (*SI Appendix*, Fig. S8*A*), the distribution of VGLUT2 cluster sizes did not change substantially across conditions, including the MeCP2$^{-/y}$ samples (*SI Appendix*, Fig. S8*B*).

Discussion

Here, we extended our serial-section STORM imaging platform to allow substantially (~10-fold) faster volumetric superresolution imaging. This in turn enabled quantitative characterization of the structural organization of the PNNs and perforating somatic synaptic contacts onto many PV+ cells, at multiple developmental stages, and under a variety of conditions of sensory and genetic perturbations.

We observed a wide range of PNN structures surrounding PV+ cells even within adult wild-type animals, ranging from a sparse, disconnected pattern to a dense and completely interconnected network that fully enmeshed the cell body and proximal dendrites. Notably, a range of immature net structures was still visible at P90, an age that is well past the critical period for plasticity in mouse V1. Likewise, the synaptic signal strengths also showed substantial cell-to-cell variability at P90, and the inhibitory synaptic signal was positively correlated with the maturational level of the PNN at the single-cell level. As the condensed PNN acts as a brake on plasticity (2, 11, 13), the presence of immature PNNs and synaptic signals around some PV+ cells in the adult animals may reflect a route for continued plasticity later in life, albeit at lower levels than during the critical period.

The maturation of PNNs involves an increased molecular structuring of chondroitin sulfate proteoglycans, yielding morphological changes that can be regulated bidirectionally by genes and experience. Our superresolution imaging identified a structural trajectory in the principal-component space for this PNN development, and the PNN maturation was correlated with Syt2 signals in recurrent inhibitory connections between PV+ cells. Total visual deprivation from birth produced moderately less developed PNNs, while PNN formation was accelerated in mice depleted of *MeCP2*, the causative gene for Rett syndrome (26, 27). Remarkably, despite changes in the overall maturation level, neither perturbation derailed the stereotypical structural trajectory of PNN assembly observed in the principal-component space. Thus, our results suggest a robust structural evolution pathway for PNN maturation: The sensory and genetic perturbations investigated do not lead to substantial deviation from this pathway but rather affect the rate or timing of maturation.

In contrast to the positive correlation observed between the PNN signal and the Syt2 signal (indicative of recurrent PV-to-PV inhibitory inputs), the VGLUT2+ signal onto PV+ cells (likely representing excitatory thalamocortical input) did not correlate with PNN maturation. Moreover, unlike the observed increase in Syt2 surface intensity on PV+ cells with age, the VGLUT2 surface intensity on PV+ cells decreased with age instead. Although our current analysis did not consider the contribution of corticocortical excitatory inputs or inputs from other modulatory sources impinging on PV+ cells, our comparison of thalamocortical excitatory inputs to PV+ cells and reciprocal PV–PV inhibitory inputs suggests a shift in excitatory–inhibitory (E–I) balance onto PV+ somata that could yield weaker PV activation and hence overall lower inhibitory output from these cells, and thus greater surrounding cortical network activity as the animal matures. Future studies are needed to explore the relative contributions of excitatory intracortical, thalamocortical, or neuromodulatory inputs to PV cells during prolonged periods of sensory deprivation.

Unlike normal development, the absence of *MeCP2* caused a shift in E–I balance that appears to favor PV+ cell activation. Specifically, we observed weaker Syt2 surface intensity and stronger VGLUT2 surface intensity on PV+ cells, suggesting weaker recurrent inhibitory input between PV+ cells and stronger excitatory thalamocortical input onto PV+ cells in *MeCP2*-deficient animals. Misregulation of synaptic inputs onto PV+ cells has recently also been observed in layer II of somatosensory and motor cortices of *MeCP2*-deficient mice, including increased intracortical excitatory synapses marked by VGLUT1 and decreased inhibitory synapses marked by vesicular GABA transporter (VGAT) onto the dendrites (but not somata) of PV+ cells (37). Despite differences in specific synaptic markers and brain regions studied, both this study and our study support a shift in balance toward greater PV+ cell activation and hence stronger inhibitory output from *MeCP2*-deficient PV+ networks onto nearby excitatory pyramidal cells. This enhanced PV+ cell activation likely contributes to the gradual dampening of global cortical network activity seen in this mouse model of Rett syndrome (34, 38, 39), as well as the hypermature PV+ axonal plexus reported previously for such a model (15, 34).

Our observation of weaker recurrent Syt2+ contacts specifically between PV+ cells in *MeCP2*-deficient animals may underlie their larger spontaneous inhibitory currents and diminished evoked inhibitory current amplitude and synaptic depression during trains of action potentials in V1 (15). Indeed, Syt2 deletion or mutation has been reported to reduce evoked synaptic response and synaptic depression as well as increase the frequency of spontaneous events at a variety of fast synapses (40, 41). We further observed substantial loss of Syt2 in the interbouton regions of axons in *MeCP2*-deficient animals, potentially implicating impaired molecular localization or

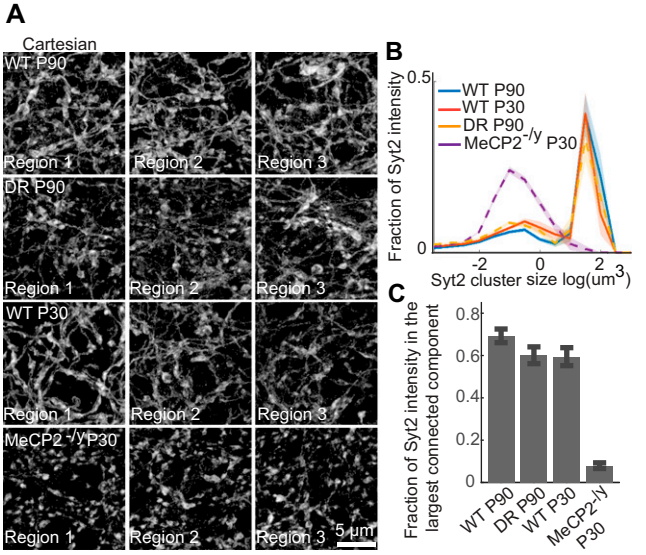

Fig. 5. Morphology of the Syt2 signal surrounding PV+ cells is altered in MeCP2$^{-/y}$ mice. (*A*) Maximum-intensity projection STORM images of the Syt2 signal around representative WFA+ PV+ cells in animals across four conditions: WT P90 (first row), WT P30 (third row), DR P90 (second row), and MeCP2$^{-/y}$ P30 (fourth row). The images are presented in Cartesian coordinates. To reduce the background in the Syt2 maximum-intensity projections through thick volumes of tissue (5 μm), small clusters <70 nm^3 in volume were removed. (*B*) Distributions of Syt2 cluster sizes for WT P90 (blue), WT P30 (red), DR P90 (yellow), and MeCP2$^{-/y}$ P30 (purple) samples for the regions surrounding each WFA+ PV+ cell. Data are plotted as the mean across imaged regions, with the SEM shown as shaded regions (n = 17 to 22 regions for each condition). (*C*) Fraction of Syt2 signals within each region that is in the largest connected component for WT P90, WT P30, DR P90, and MeCP2$^{-/y}$ P30 samples. The graph shows the mean across the imaged regions, and the error bars are the SEM (n = 17 to 22 regions for each condition).

transport in PV+ cells. Notably, these Syt2 defects on PV+ cells were observed at a stage just before loss of visual function (34, 35), suggesting a potential early circuit signature for Rett syndrome to be verified in heterozygous female mice and patients.

We envision that the volumetric superresolution imaging platform reported here, which allows molecular imaging with nanometer-scale resolution across large tissue volumes, can be applied to track the pathogenesis of a variety of mental illnesses linked to disruptions in neuronal networks and the extracellular matrix (5, 6, 42, 43) and, more broadly, to elucidate the structural changes of the brain both during normal development and in disease.

Materials and Methods

Tissue sections containing primary visual cortex were fixed, stained with antibodies and lectins, and then embedded in epoxy resin. Arrays of ultrathin sections of the embedded tissue were imaged using a custom-built, automated STORM microscope. Three-dimensional images were reconstructed from serial ultrathin sections and used for further analysis. Additional detailed descriptions including experimental models, sample preparation, superresolution imaging, volumetric image reconstruction, and data analysis can be found in *SI Appendix, Materials and Methods*.

Animal work was performed in accordance with protocols approved by the Institutional Animal Care and Use Committee at Harvard University and in compliance with all ethical regulations.

ACKNOWLEDGMENTS. We thank N. DeSouza for animal care and maintenance, and C. Speer, J. Moffitt, and M. Fagiolini (Grant R01 NS095959) for discussions during the course of the project. This work was supported in part by the NIMH Silvio O. Conte Center (Grant P50MH094271 to T.K.H. and X.Z.) and NIH (Grant R35GM122487 to X.Z.). X.Z. is a Howard Hughes Medical Institute Investigator.

1. Hensch TK (2004) Critical period regulation. *Annu Rev Neurosci* 27:549–579.
2. Takesian AE, Hensch TK (2013) Balancing plasticity/stability across brain development. *Prog Brain Res* 207:3–34.
3. Levelt CN, Hübener M (2012) Critical-period plasticity in the visual cortex. *Annu Rev Neurosci* 35:309–330.
4. Hu H, Gan J, Jonas P (2014) Interneurons. Fast-spiking, parvalbumin^{+} GABAergic interneurons: From cellular design to microcircuit function. *Science* 345:1255263.
5. Do KQ, Cuenod M, Hensch TK (2015) Targeting oxidative stress and aberrant critical period plasticity in the developmental trajectory to schizophrenia. *Schizophr Bull* 41: 835–846.
6. Marín O (2016) Developmental timing and critical windows for the treatment of psychiatric disorders. *Nat Med* 22:1229–1238.
7. Celio MR, Spreafico R, De Biasi S, Vitellaro-Zuccarello L (1998) Perineuronal nets: Past and present. *Trends Neurosci* 21:510–515.
8. Miyata S, Komatsu Y, Yoshimura Y, Taya C, Kitagawa H (2012) Persistent cortical plasticity by upregulation of chondroitin 6-sulfation. *Nat Neurosci* 15:414–422, S1–S2.
9. Favuzzi E, et al. (2017) Activity-dependent gating of parvalbumin interneuron function by the perineuronal net protein brevican. *Neuron* 95:639–655.e10.
10. Hockfield S, Kalb RG, Zaremba S, Fryer H (1990) Expression of neural proteoglycans correlates with the acquisition of mature neuronal properties in the mammalian brain. *Cold Spring Harb Symp Quant Biol* 55:505–514.
11. Wang D, Fawcett J (2012) The perineuronal net and the control of CNS plasticity. *Cell Tissue Res* 349:147–160.
12. Brückner G, et al. (1998) Acute and long-lasting changes in extracellular-matrix chondroitin-sulphate proteoglycans induced by injection of chondroitinase ABC in the adult rat brain. *Exp Brain Res* 121:300–310.
13. Pizzorusso T, et al. (2002) Reactivation of ocular dominance plasticity in the adult visual cortex. *Science* 298:1248–1251.
14. Krencik R, et al. (2015) Dysregulation of astrocyte extracellular signaling in Costello syndrome. *Sci Transl Med* 7:286ra66.
15. Krishnan K, et al. (2015) MeCP2 regulates the timing of critical period plasticity that shapes functional connectivity in primary visual cortex. *Proc Natl Acad Sci USA* 112: E4782–E4791.
16. Mauney SA, et al. (2013) Developmental pattern of perineuronal nets in the human prefrontal cortex and their deficit in schizophrenia. *Biol Psychiatry* 74:427–435.
17. Frischknecht R, et al. (2009) Brain extracellular matrix affects AMPA receptor lateral mobility and short-term synaptic plasticity. *Nat Neurosci* 12:897–904.
18. Beurdeley M, et al. (2012) Otx2 binding to perineuronal nets persistently regulates plasticity in the mature visual cortex. *J Neurosci* 32:9429–9437.
19. Vo T, et al. (2013) The chemorepulsive axon guidance protein semaphorin3A is a constituent of perineuronal nets in the adult rodent brain. *Mol Cell Neurosci* 56: 186–200.
20. Cabungcal JH, et al. (2013) Perineuronal nets protect fast-spiking interneurons against oxidative stress. *Proc Natl Acad Sci USA* 110:9130–9135.
21. Cabungcal JH, et al. (2014) Juvenile antioxidant treatment prevents adult deficits in a developmental model of schizophrenia. *Neuron* 83:1073–1084.
22. Tsien RY (2013) Very long-term memories may be stored in the pattern of holes in the perineuronal net. *Proc Natl Acad Sci USA* 110:12456–12461.
23. Rust MJ, Bates M, Zhuang X (2006) Sub-diffraction-limit imaging by stochastic optical reconstruction microscopy (STORM). *Nat Methods* 3:793–795.
24. Punge A, et al. (2008) 3D reconstruction of high-resolution STED microscope images. *Microsc Res Tech* 71:644–650.
25. Sigal YM, Speer CM, Babcock HP, Zhuang X (2015) Mapping synaptic input fields of neurons with super-resolution imaging. *Cell* 163:493–505.
26. Amir RE, et al. (1999) Rett syndrome is caused by mutations in X-linked MECP2, encoding methyl-CpG-binding protein 2. *Nat Genet* 23:185–188.
27. Guy J, Hendrich B, Holmes M, Martin JE, Bird A (2001) A mouse Mecp2-null mutation causes neurological symptoms that mimic Rett syndrome. *Nat Genet* 27:322–326.
28. Härtig W, Brauer K, Brückner G (1992) Wisteria floribunda agglutinin-labelled nets surround parvalbumin-containing neurons. *Neuroreport* 3:869–872.
29. Fremeau RT, Jr, et al. (2001) The expression of vesicular glutamate transporters defines two classes of excitatory synapse. *Neuron* 31:247–260.
30. Geppert M, Archer BT, III, Südhof TC (1991) Synaptotagmin II. A novel differentially distributed form of synaptotagmin. *J Biol Chem* 266:13548–13552.
31. Sommeijer JP, Levelt CN (2012) Synaptotagmin-2 is a reliable marker for parvalbumin positive inhibitory boutons in the mouse visual cortex. *PLoS One* 7:e35323.
32. Fagiolini M, Pizzorusso T, Berardi N, Domenici L, Maffei L (1994) Functional postnatal development of the rat primary visual cortex and the role of visual experience: Dark rearing and monocular deprivation. *Vision Res* 34:709–720.
33. Kang E, et al. (2013) Visual acuity development and plasticity in the absence of sensory experience. *J Neurosci* 33:17789–17796.
34. Durand S, et al. (2012) NMDA receptor regulation prevents regression of visual cortical function in the absence of Mecp2. *Neuron* 76:1078–1090.
35. LeBlanc JJ, et al. (2015) Visual evoked potentials detect cortical processing deficits in Rett syndrome. *Ann Neurol* 78:775–786.
36. Kameda H, et al. (2012) Parvalbumin-producing cortical interneurons receive inhibitory inputs on proximal portions and cortical excitatory inputs on distal dendrites. *Eur J Neurosci* 35:838–854.
37. Morello N, et al. (2018) Loss of Mecp2 causes atypical synaptic and molecular plasticity of parvalbumin-expressing interneurons reflecting Rett syndrome-like sensorimotor defects. *eNeuro* 5:ENEURO.0086-18.2018.
38. Kron M, et al. (2012) Brain activity mapping in Mecp2 mutant mice reveals functional deficits in forebrain circuits, including key nodes in the default mode network, that are reversed with ketamine treatment. *J Neurosci* 32:13860–13872.
39. Liao W, Gandal MJ, Ehrlichman RS, Siegel SJ, Carlson GC (2012) MeCP2+/- mouse model of RTT reproduces auditory phenotypes associated with Rett syndrome and replicate select EEG endophenotypes of autism spectrum disorder. *Neurobiol Dis* 46: 88–92.
40. Pang ZP, Sun J, Rizo J, Maximov A, Südhof TC (2006) Genetic analysis of synaptotagmin 2 in spontaneous and Ca^{2+}-triggered neurotransmitter release. *EMBO J* 25: 2039–2050.
41. Chen C, Arai I, Satterfield R, Young SM, Jr, Jonas P (2017) Synaptotagmin 2 is the fast Ca^{2+} sensor at a central inhibitory synapse. *Cell Rep* 18:723–736.
42. Steullet P, et al. (2017) Oxidative stress-driven parvalbumin interneuron impairment as a common mechanism in models of schizophrenia. *Mol Psychiatry* 22:936–943.
43. Sorg BA, et al. (2016) Casting a wide net: Role of perineuronal nets in neural plasticity. *J Neurosci* 36:11459–11468.